This is the peer reviewd version of the followng article:

27/12/2024 04:28

(Article begins on next page)

Fracture density variations within a reservoir-scale normal fault zone: A case study from shallow-water carbonates of southern Italy

Giovanni Camanni [a,*], Francesco Vinci [a,b], Stefano Tavani [a,c], Valeria Ferrandino [a], Stefano Mazzoli [e], Amerigo Corradetti [d], Mariano Parente [a], Alessandro Iannace [a]

[a] *DiSTAR, Università degli Studi di Napoli Federico II, Naples, Italy*
[b] *PanTerra Geoconsultants, Leiderdorp, the Netherlands*
[c] *Consiglio Nazionale delle Ricerche, IGAG, Rome, Italy*
[d] *Dipartimento di Matematica e Geoscienze, Università di Trieste, Trieste, Italy*
[e] *School of Science and Technology - Geology Division, University of Camerino, Camerino, Italy*

ABSTRACT

Fault zones can often display a complex internal structure associated with antithetic faults, branch and tip points, bed rotations, bed-parallel slip surfaces, and subordinate synthetic faults. We explore how these structural complexities may affect the development of fault-related fractures as displacement accumulates. We analysed in detail an incipient fault zone within well-bedded, shallow-water carbonates of the southern Apennines thrust belt (Italy). The fault zone crops out with quasi-complete exposure at a reservoir scale on an inaccessible sub-vertical cliff face, and fault and fracture mapping were carried out on a 3D virtual outcrop model of the exposure built for this study using photogrammetry. Comparing the structure of the fault zone and the density of 9444 mapped fractures allowed us to unravel their spatial relationships. Our results show that the areas of denser fractures coincide with: (i) rock volumes bounded by antithetic faults developed within the fault zone, (ii) branch points between these antithetic faults and fault zone-bounding fault segments, (iii) fault zone-bounding fault segments associated with significant displacement gradients, and (iv) relay zones between subordinate synthetic faults. These findings may aid locating sub-seismic resolution volumes of dense fracturing and associated enhanced permeability within faulted reservoirs.

1. Introduction

Normal faults rarely occur as individual planar surfaces and mostly comprise multiple synthetic fault segments (Walsh and Watterson, 1989; Childs et al., 1996, 2009; Peacock, 2002; Marchal et al., 2003; Walsh et al., 2003; Kristensen et al., 2008; Delogkos et al., 2020). Within such segmented faults, portions bounded by two synthetic, adjacent fault segments or individual slip surfaces enclosed by a zone of lower shear strain faults and fractures, are often referred to as "fault zones" (e.g., Peacock et al., 2000; Childs et al., 2009; Faulkner et al., 2010; Ferrill et al., 2011). Furthermore, in circumstances in which it can be demonstrated that displacement is transferred between two synthetic, adjacent fault segments, the rock volume they bound is referred to with the more specific term of "relay zone" (Peacock and Sanderson, 1991, 1994; Childs et al., 1995; Huggins et al., 1995; Camanni et al., 2019; Nicol et al., 2020; Roche et al., 2020, 2021). Relay and fault zones can display

a complex internal structure comprising, among other features, antithetic faults, branch and tip points, bed rotations, bed-parallel slip surfaces, as well as subordinate synthetic faults (Mandl, 1987; Ferrill and Morris, 2008; Van der Zee et al., 2008; Childs et al., 2009; Ferrill et al., 2011; Zaky, 2017; Delogkos et al., 2017a, b, 2018; Nixon et al., 2018; Nabavi et al., 2020).

As displacement accumulates on normal faults, it has been shown that their segmentation can variably influence the spatial distribution of fractures and fault rock (Aarland and Skjerven, 1998; Rotevatn et al., 2007; Childs et al., 2009; Michie, 2015; Michie and Haines, 2016). For example, it has been demonstrated that shear strain can be greatest in relay zones between adjacent fault segments (Fossen et al., 2005; Rotevatn et al., 2007; Childs et al., 2009; Nixon et al., 2018, 2020; Mercuri et al., 2020). Furthermore, with increasing displacement these relay zones breach (e.g., Peacock and Sanderson, 1991; 1994; Childs et al., 1995; 2009; Crider and Pollard, 1998; Peacock, 2002; Soliva and

---

Benedicto, 2004), and can eventually form fault-bound lenses of fault rock (Childs et al., 2009). However, it is still poorly understood how, at the scale of individual relay and fault zones, fault-related fractures are spatially distributed and how their density may relate to the complex internal structure that relay and fault zones can display.

In this study we conducted a detailed analysis of an incipient normal fault zone developed in carbonates and preserving a broad spectrum of internal, structural complexities. These are: antithetic faults, branch points between these antithetic faults and fault zone-bounding fault segments, fault segments tipping out and associated with significant displacement gradients, and relay zones between subordinate synthetic faults. The fault zone crops out at a reservoir scale, and with its entire width and a significant part of its height fully exposed, allowing very detailed mapping not only of its structure, but also of fractures within it. The structure of the fault zone and the density of fractures were compared to one another to investigate whether a spatial relationship between them existed.

2. Geological setting

The study area is located in the southern Apennines fold and thrust belt of Italy, a Neogene belt consisting of a stack of NE-verging nappes, each deforming distinct Mesozoic-Paleogene paleogeographic domains (Roure et al., 1991; Cello and Mazzoli, 1999; Menardi Noguera and Rea, 2000). The outcrop analysed in this work is exposed within the carbonate succession of the Apennine Carbonate Platform (D'Argenio et al., 1975), one of the major nappes of the tectonic pile, and is located near the Catiello peak in the Lattari Mountains of the Sorrento Peninsula (Fig. 1). The Lattari Mountains are mainly made of Upper Triassic to Upper Cretaceous shallow-water limestones and dolostones (De Castro, 1962; Robson, 1987; Iannace, 1993; Carannante et al., 2000; Iannace et al., 2011, 2014; Vinci et al., 2017), unconformably overlain by Miocene foredeep and wedge-top basin successions (including sandstones, calcareous sandstones, and conglomerates). The entire sedimentary pile is locally covered by Quaternary pyroclastic deposits (Fig. 1; ISPRA, 2016). The carbonate succession of the Lattari Mountains
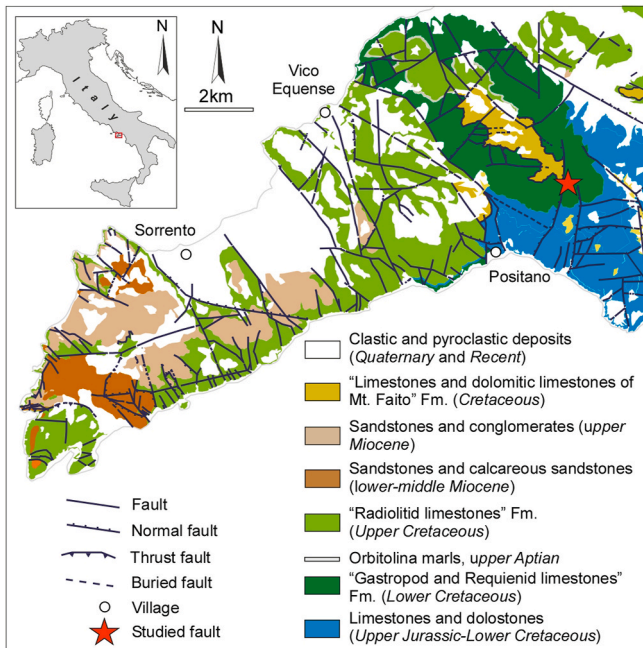

Fig. 1. Geological map of the Sorrento Peninsula in the southern Apennines fold and thrust belt (modified after ISPRA, 2016). Inset shows location of the map in southern Italy. Note location of the studied fault highlighted with a red star in the geological map. (For interpretation of the references to colour in this figure legend, the reader is referred to the Web version of this article.)

is affected by high angle faults (Fig. 1) and by a background fracture network consisting of dominantly bedding-perpendicular joints (e.g., Milia and Torrente, 1997; Caiazzo et al., 2000; Guerriero et al., 2010, 2011; Perriello Zampelli et al., 2015; Corradetti et al., 2018).

The outcrop studied (Fig. 2A) exposes a gently NE-ward dipping succession comprising alternating shallow-water limestones and dolostones belonging to the Lower Cretaceous "Gastropods and Requienid limestones" ("Calcari con Requienie e Gasteropodi") Formation (Fig. 1). Within the study outcrop, the stratigraphic succession includes two main units (Vinci et al., 2017): an upper unit of thinly-bedded limestones and dolostones ("C" interval of Vinci et al., 2017), and a lower unit mostly comprising thinly-bedded dolostones ("B" interval of Vinci et al., 2017). The boundary between the two stratigraphic units is marked by a well-defined break in the cliff slope, due to differential erosion of the two lithologies (Fig. 2A).

3. Methodological approach

The outcrop studied consists of a mostly inaccessible cliff face nearly 250 m in height and 100 m in width. To study faulting and fracturing in the cliff, we used field acquisition of digital images collected by an unmanned aerial vehicle (UAV), designed to generate a 3D virtual outcrop model (VOM). Subsequently, fault and fracture mapping were carried out on both the 3D model and 2D orthorectified images. The resulting maps were used to determine the density of fractures. Detailed descriptions of each of these methodological steps are outlined in the following sections.

3.1. Data acquisition and construction of the virtual outcrop model

The initial phase of this study was aimed at the construction of the VOM of the study outcrop, which was carried out by means of structure from motion-multi view stereo (SfM-MVS) photogrammetric techniques (Westoby et al., 2012). This is a fairly common technique in Earth Sciences, and consists of reconstructing a 3D object through the analysis of multiple, partly overlapping images of the same scene taken from different points of view (Remondino and El-Hakim, 2006). Due to the rough outcrop topography, as well as its large size (ca. 250 m × 100 ;m), we acquired photos by UAV. The UAV was equipped with a digital photo-camera Sony Alpha 7r, with a sensor of 7360 × 4912 pixel and a lens Sonnar/carl-zeiss of 35 mm f2.8, that allowed to collect photos of 36 Mpixels each.

To build the VOM, a selection of 173 digital photos was input into the Agisoft Metashape photogrammetry package. After the SFM-WMS workflow, a dense point-cloud consisting of ~23.8 × 10^6 points, was created and used to build a mesh of ~44.5 × 10^6 triangles. A texture map was draped onto the triangular mesh, in order to obtain a photo-realistic VOM. Finally, the model was geo-referenced using seven ground control points located by differential GNSS antenna. The final VOM comprises of a surface of ~3.93 × 10^4 m^2 with a resolution in the original point cloud of ~0.6 point/cm^2. An orthophoto of the final VOM was also exported, using a view direction approximately orthogonal to the strike of the main faults, to aid fault and fracture mapping (Fig. 2A, and Supplementary Fig. 1).

3.2. Fault and fracture mapping

To map the faults and the fractures, the VOM was imported into 3DMove and OpenPlot (Tavani et al., 2011) software, respectively. Fault segments and horizons were mapped to estimate fault throws. Mapping was initially carried out in the 3DMove environment, and successively refined in 2D using the orthophoto of the VOM, and some individual high-resolution photos collected from the UAV during data acquisition.

Fractures were digitized on the VOM within the 3D environment of OpenPlot, which permitted creation of planar polygons used to extract dip and strike of each digitized fracture. Only fractures with heights
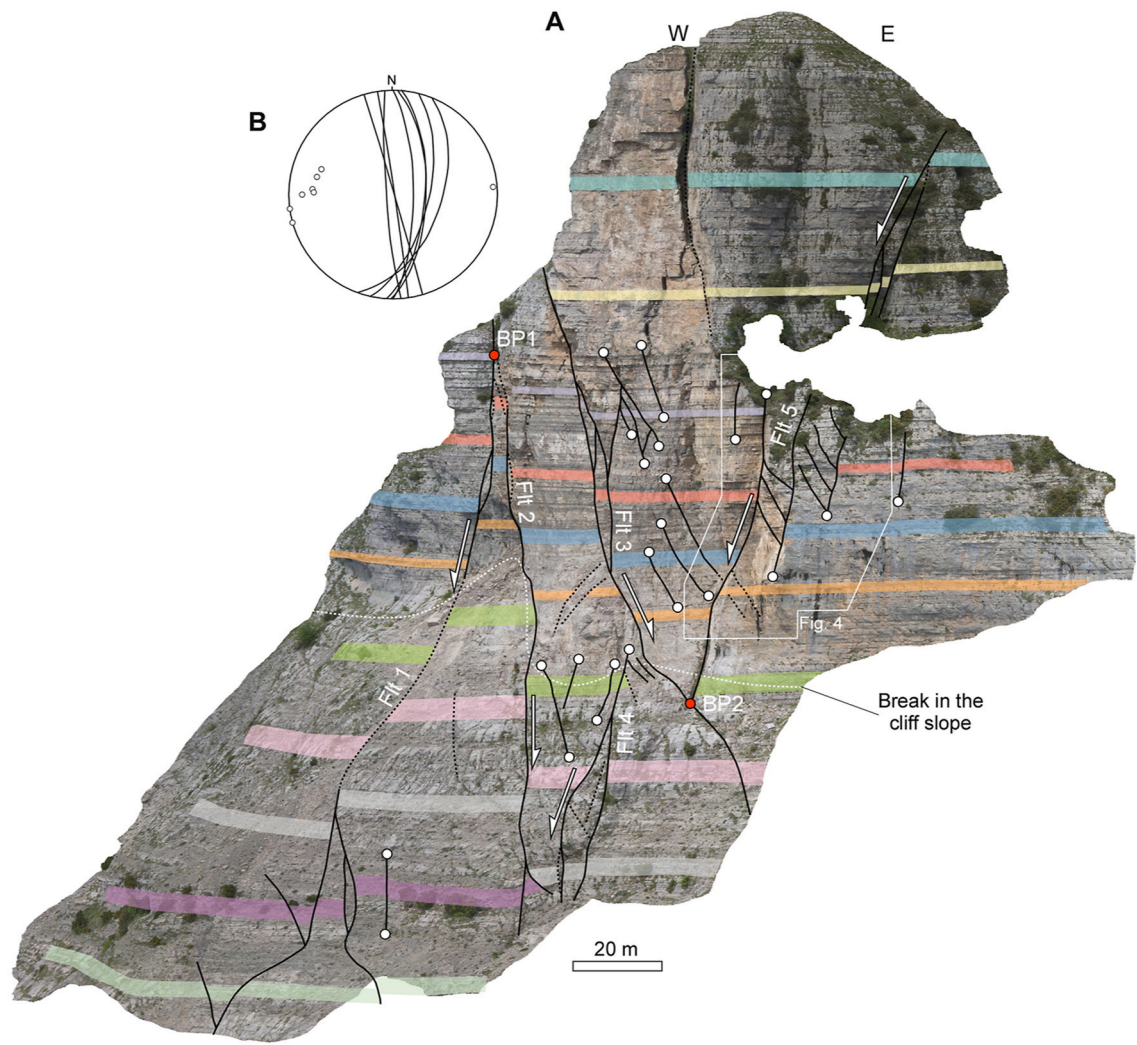
Fig. 2. A: Fault interpretation and drawing of selected marker horizons on the orthophoto exported from the VOM in a direction nearly orthogonal to the strike of the main faults. White dots are fault tip points, while red dots show main branch points between opposed-dipping faults. The dotted white line highlights the break in the cliff topography, which is steeper in the upper limestone unit (made up of thinly-bedded limestones and dolostones) than in the lower one (made up of thinly-bedded dolostones). B: orientation of faults indicated as great circles and poles in the lower hemisphere, equal-area projection (N = 8). (For interpretation of the references to colour in this figure legend, the reader is referred to the Web version of this article.)

greater than 20 cm were mapped as, within the study area, the orientation of a fracture cannot be reliably measured from the VOM for shorter fractures.

3.3. Fracture density analysis

Fracture traces were extracted from OpenPlot in. txt node format and were input into the MATLAB™ toolbox FracPaQ *v.* 2.8 (Healy et al., 2017), where fracture traces were used for performing spatial fracture analysis. This analysis consisted, for the scope of this article, in determining their density, labelled P20 by Dershowitz and Herda (1992). Fracture density is defined as the number of fractures per unit area, and was determined using the circular scan window method of Mauldon et al. (2001). According to this method, fracture density is estimated as:

$$m/2\pi r^2$$

where m is the number of fractures terminating within a circle of radius r. FracPaQ generated a 2D grid of evenly spaced circular scan windows to fit within the fracture trace map area, where the scan circle diameter is defined as 0.99 of the grid spacing in x and y in order to avoid overlapping scan circles. The choice of an appropriate scan circle size is key

to adequately capture the spatial distribution of fractures, since it can greatly influence fracture densities. In literature it is suggested that, as rule of thumb, the chosen scan circle size should be sufficient to achieve a minimum of 30 fracture terminations per circle (Rohrbaugh et al., 2002; Zeeb et al., 2013). For the outcrop area mapped in this article, the number of the scan circles was 10 along the horizontal axis, 15 along the vertical axis, and their radius was 7.34 m. This scan circle size allowed a meaningful sampling of fractures as each scan circle is large enough to contain at least a few tens of fractures, but it is also small enough to create a grid with a number of elements sufficient for adequately capturing the spatial variability in the distribution of fractures within the study area. We are aware that some scan circles will include a larger number of fractures than others, but this is inevitable due to the irregular borders of the data extent. Furthermore, a scan circle radius of 7.34 m is roughly one order of magnitude smaller than the average fault height in the study area, and it is therefore suitable for comparing the two sets of structures. Fractures were then gridded in box-shaped bins corresponding to the locations of the scan circles to produce a fracture density map.

4. Results

4.1. Faults

The outcrop studied is affected by five nearly N–S-striking, steeply dipping, and variably segmented faults with normal displacements (Fig. 2A and B). Although no kinematic data are directly available from the outcrop due to its inaccessibility, we interpret these extensional displacements to be predominantly dip-slip, consistent with the kinematics of similar faults in adjacent areas (e.g., Milia and Torrente, 1997; Caiazzo et al., 2000). The mapped normal faults are parallel to N–S and orthogonal to E-W striking tension fractures forming the two dominant joint sets in the region (Corradetti et al., 2018). Faults are associated with several tens of meters heights and are either dipping to the west (faults Flt1, Flt4 and Flt5) or to the east (faults Flt2 and Flt3). However, we stress that this non-fractal distribution of fault sizes is apparent as smaller faults can be also noted within the outcrop and larger faults can be expected to occur at a scale larger than that of the outcrop. Despite showing opposite dip directions, W-dipping and E-dipping faults are structurally linked to one another at well-defined branch points (red dots in Fig. 2A). Faults Flt1 and Flt2 link upward at the branch point BP1, located near the boundary of the analysed surface exposure, while faults Flt3 and Flt5 are linked at the branch point BP2, located near the break in the cliff slope (Fig. 2A). Furthermore, faults Flt2 and Flt4 are approaching one another at the bottom part of the outcrop, suggesting that they may also link at a branch point located outside the study area.

All five faults accommodate several meters throw, and each fault is associated with a characteristic throw distribution (Fig. 3). For example, fault Flt1, after a sudden increase in throw from nearly 8 m to nearly 9 m near its upper branch point BP1 with fault Flt2, displays a well-defined throw gradient associated with an overall downwards decrease in throw. Throw on fault Flt1 reaches values as low as ca. 2 m at the bottom of the outcrop, where the fault bifurcates downward into two segments. In contrast, fault Flt2, the largest throw fault in the outcrop, is associated with a constant throw of ca. 16 m along its entire sampled height. Fault Flt3 has a roughly constant throw of ca. 5 m along most of its height, with minor variations of < than 1 m. However, at its branch point BP2 with fault Flt5, fault Flt3 displays a rapid decrease of throw from ca. 5 m to ca. 1 m. Fault Flt4, which comprises two segments that link upward, displays a downward increase in throw from null values at its upper tip, to a throw of ca. 2 m at the base of the investigated outcrop surface. Finally, throw across fault Flt5 has values of ca. 5–6 m.

The total throw calculated by summing the throw of individual faults along the outcrop vertical extent (Fig. 3) has a nearly constant magnitude in the central part of the outcrop where throws of all 5 faults are readily measurable. However, the total throw decreases upward and downward along the outcrop where faults extend outside the data extent and, therefore, throws are not detectable.

Fault Flt 5 (Figs. 2A and 4) comprises three synthetic steep westward-dipping fault segments, which bound zones associated with antithetic faulting and local synthetic bed rotation (Fig. 4). All three synthetic fault segments have at least one tip within the study area. Interestingly, the westernmost segment increases downward in throw from its upper tip point, and this is accompanied by a downward decrease in throw along the fault segment in its immediate footwall. These displacement changes indicate that throw is transferred between the two fault segments, and
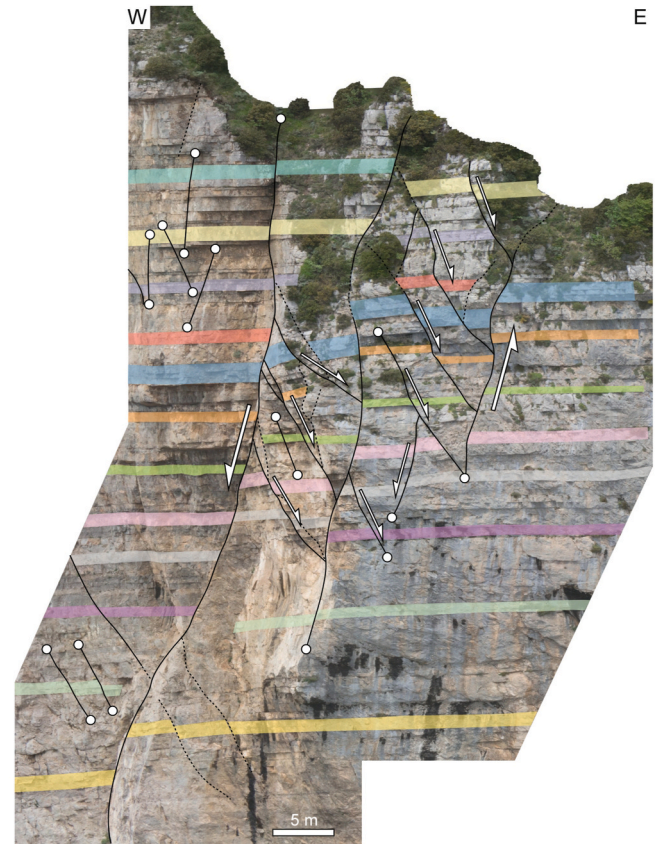

Fig. 4. Interpretation and drawing of selected marker horizons on the ortho-photo exported from the VOM in a direction nearly orthogonal to the strike of the main fault segments for the highly segmented portion of fault Flt 5. The location of the area of this figure is indicated in Fig. 2 B. White dots show fault tip points.
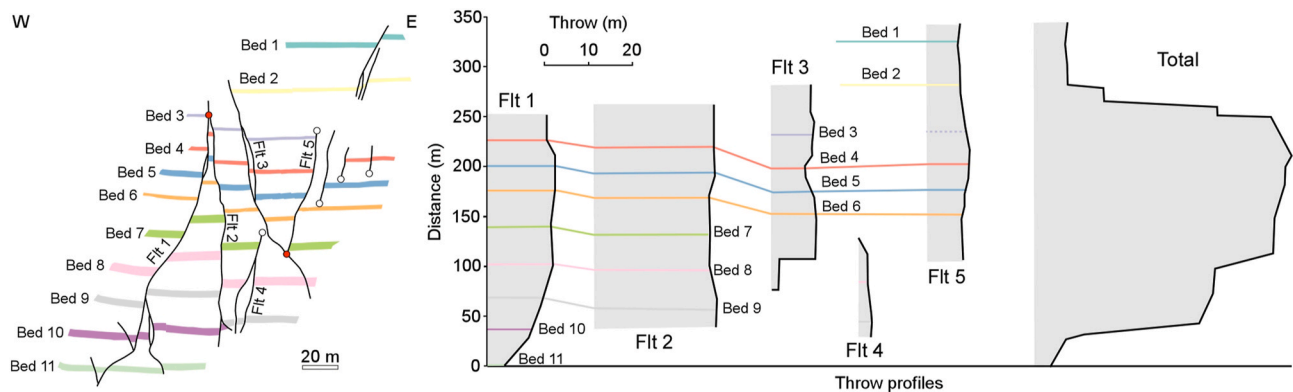

Fig. 3. Throw profiles for the faults comprised in the outcrop. The starting point for measuring distances for building these profiles has been taken to coincide with their upper end of data (i.e., faults Flts 2, 3 and 5), tip (i.e., fault Flt 4) or branch (i.e., fault Flt 1) points. The location of some key beds illustrated in the sketch in the left is also shown on the throw profiles. Note that for building these profiles throw values of many more markers horizons than those shown have been used.

that the rock volume between segments, associated with several antithetic faults, forms a contractional a relay zone (e.g., Camanni et al., 2019 and references therein). Finally, the easternmost segment of fault Flt5 is also associated with a downward decrease in throw, which cannot be directly associated with throw transfer between this fault segment and the segment in its hanging wall, as both tip out downward.

4.2. Fractures

A total of 9444 fractures were mapped and digitized within the VOM (Figs. 5 and 6A). Inspection of fracture orientations (Fig. 5) indicates that they are steeply dipping, with some strike maxima of ENE-WSW, ESE-WNW, and NNW-SSE. In the next paragraph, we will describe the main features associated with the spatial distribution of the density of fractures (Fig. 6B) from east to west, with reference to the location of the faults previously described, and to the location of the break in the cliff slope (dashed black line in Fig. 6B).

An area of nearly null fracture densities can be identified east of fault Flt5. The highly segmented central portion of fault Flt5, whose structure is detailed in Fig. 4, is associated with larger fracture density values (P20 up to nearly 0.2 m^{-2}). West of fault Flt5, density values of ca. 0.1 to 0.3 m^{-2} define a roughly triangular area bounded to the west by fault Flt3. Within this triangular zone, a maximum fracture density occurs in the hanging wall of fault Flt5, reaching values of 0.5 m^{-2} in the uppermost part of the study area. Fault Flt3 is associated with a westward increasing gradient in fracture density values, with the P20 parameter spanning from roughly 0.2 m^{-2} to around 0.4 to 0.5 m^{-2} above the break in the cliff slope, and from 0 to 0.1 m^{-2} to ca. 0.3 m^{-2} below it. In the area between faults Flt3 and Flt1, which includes fault Flt2, P20 values range overall between 0.3 and 0.5 m^{-2}, with some minima occurring around the zones of no data, and some local maxima. One of these maxima occurs between faults Flt2 and Flt3. This maximum has fracture densities of ca. 0.6 m^{-2} above the break in the cliff slope and values as high as ca. 1 m^{-2} near the uppermost boundary of the study area. Another

maximum, associated with P20 values of up to ca. 0.6 m^{-2}, occurs near the intersection of faults Flt4 and Flt2. However, the most striking maximum occurs around the branch point BP1 between faults Flt1 and Flt2 and is associated with values of P20 up to at least 2 m^{-2}. Finally, the area west of fault Flt1 is associated with fracture density values higher than 0.5 m^{-2}, locally reaching magnitudes in excess of 1.2 m^{-2}.

5. Discussion

5.1. An incipient fault zone

The five faults that we recognised within the studied outcrop, although displaying diverse dip angle values and accommodating various amounts of displacement, appear to be related in several ways. Firstly, their displacements sum up to one another to give rise to a bulk nearly constant displacement (central portion of the outcrop in Fig. 3). Furthermore, along the entire height of the outcrop exposure, across all faults, beds seem to neither downthrow significantly in W or E directions (Fig. 2A). These considerations indicate that all faults are part of a coherent array in which each has a role in maintaining roughly constant the overall amount of horizontal extension (e.g., Walsh and Watterson, 1991; Nicol et al., 2016). Secondly, faults are spatially arranged in a way that fault Flt1 to the west and faults Flt4 and Flt5 to the east bound faults Flt2 and Flt3. Thirdly, opposed-dipping faults are physically linked at well-defined branch points and abut, rather than cross-cut, one another, indicating that all faults are likely associated with the same faulting event.

According to previous studies (e.g., Peacock et al., 2000; Faulkner et al., 2003; 2010; Ferrill et al., 2011; Childs et al., 2009), all of these observations indicate that the five faults are part of a composite "fault zone". In this scenario, and considering this fault zone as a portion of a larger, segmented fault that extends beyond the outcrop extent, fault Flt1 can be envisioned as the fault segment bounding the zone in the hanging wall, while faults Flt4 and Flt5 defining the bounding fault segment in the footwall. In contrast, faults Flt2 and Flt3 can be considered to be antithetic faults developed within the fault zone. The fault zone has a maximum width (distance between faults Flt1 and Flt5 calculated normal to the fault planes) of ca. 65 m, which makes it comparable in size to those that can be mapped in high-resolution seismic reflection data.

As described in the previous paragraph, the total displacement across the fault zone is relatively small. This suggests that the fault zone as a whole is embryonal, or alternatively that we analysed a portion located near the fault tip line – where displacement would rapidly decrease – of a more evolved fault zone. In both possibilities, the analysed portion of the fault zone can be considered at an incipient stage of development. Furthermore, by comparing the structure of the fault zone (Fig. 2A) with that of the relay zone that we identified along its bounding fault segment 5 (Fig. 4), some remarkable similarities can be noticed. The relay zone in Fig. 4 is bound by two synthetic fault segments and displays an internal structure associated with antithetic faulting, similar in geometry to the larger fault zone that affects the entire outcrop. Therefore, it seems reasonable to infer that the large-scale fault zone may represent a "picture" of an early stage of development of a relay zone such as is observed in Fig. 4. However, it is beyond the scope of this article to address relay zone growth and evolution processes, and we prefer to use the more generic term "fault zone", which does not necessarily have a kinematic connotation on how displacement is transferred among bounding fault segments (e.g., Childs et al., 2009).

5.2. Spatial relationships between fault zone structure and fracture density

Most of the measured P20 (i.e., fracture density) values are at least one or two orders of magnitude smaller than the typical P20 values measured in the damage zone of carbonate faults of the Apennines (e.g.,
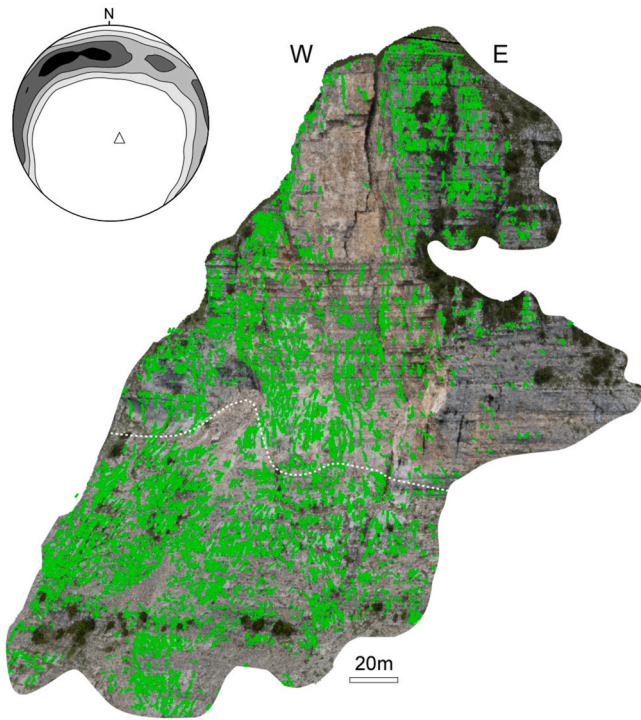

Fig. 5. Mapped fractures (N = 9444) within the VOM. The contour plot shows the principal clusters of poles to fractures. The triangle corresponds to the average pole to bedding, which is gently dipping to the NNW.
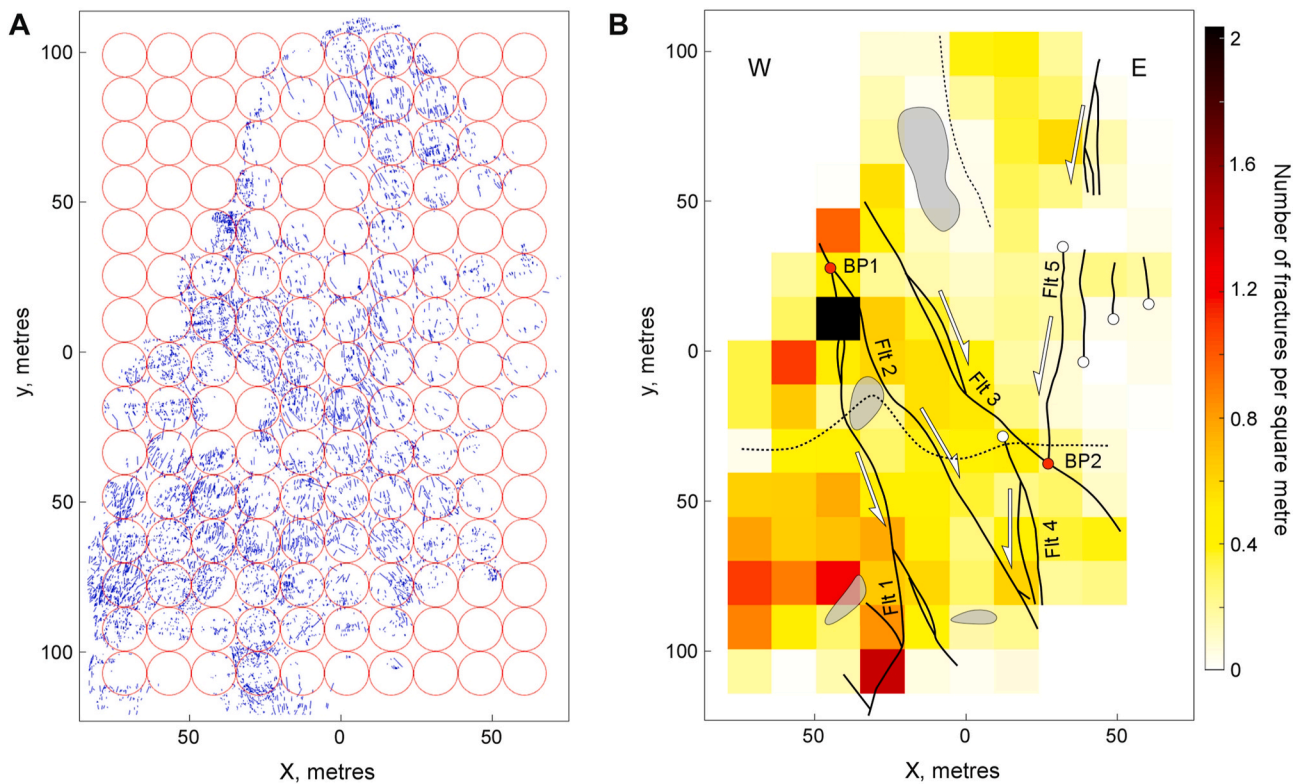
Fig. 6. Fracture traces (depicted in blue) viewed in FracPaq *v.* 2.8 software environment. A: grid of evenly spaced scan circles. Note that their number and size is defined by FracPaQ software on the basis of the extent of the fracture trace map area (in this case, 10 scan circles were constructed along the horizontal axis, and 15 along the vertical one, each with a radius of 7.34 m). B: Fracture density map of the data in A in box-shaped bins corresponding to the locations of the scan circles. The grey patches show areas of no outcrop data (e.g., highly vegetated areas, or areas covered by debris). The location of the principal faults recognised within the outcrop is indicated, together with the break in the cliff slope (dashed black line). White dots are fault tip points; red dots show the main branch points between opposed-dipping faults. (For interpretation of the references to colour in this figure legend, the reader is referred to the Web version of this article.)

Demurtas et al., 2016; Mercuri et al., 2020), supporting the embryonic nature of the studied fault zone. In this regard, occurrence of similar fractures in adjacent unfaulted carbonate cliffs (e.g., Corradetti et al., 2018), indicates that part of the studied fractures has formed during extension but before incipient faulting, and should be regarded as background fractures. We speculate that P20 values associated with these background fractures are preserved in the less fractured areas and thus we here interpret P20 values of less than ca. 0.4 m^{-2} to be associated with the pre-faulting background fracture network, while P20 values in excess of ca. 0.4 m^{-2} to be related to faulting.

Comparison of fracture data with fault zone structure indicates that highest fracture density values within the fault zone are from the area between the antithetic faults Flt2 and Flt3 (Fig. 6B). These faults both show low throw gradients (i.e., nearly constant throws), indicating that significant throw is not being transferred between them. On the other hand, the triangular areas bounded by opposed-dipping faults, such as that between the fault zone-bounding fault segment Flt1 and the antithetic fault Flt2, and that between the fault zone-bounding fault segment Flt5 and the antithetic fault Flt3, are characterised by low fracture densities (Fig. 6B). However, opposed-dipping faults seem to be associated with the development of localised areas of enhanced fracturing at their branch points, likely due to the high strains occurring at those sites (Fig. 6B).

Another local site of high fracture density (P20 of 0.5 m^{-2} to more than 1.2 m^{-2}) occurs in the hanging wall of the fault zone. Here, the fault zone-bounding fault segment Flt1 is associated with the largest and most intense zones of fracturing (Fig. 6B), although this fault accommodates a rather small throw. Fault segment Flt1 does however display a marked throw gradient from ca. 9 m (at its upper branch point BP1 with antithetic fault Flt2) to ca. 2 m at the lower edge of the study area (Figs. 2A and 3).

A similar site in which the location of dense fracturing (P20 up to nearly 0.2 m^{-2}) is associated with significant throw gradients is the centre of the fault-zone bounding fault segment Flt5 (Figs. 4 and 6B). In this area, enhanced fracturing causes a salient where very little strain occurs in the footwall of the fault zone (Fig. 6B). This salient may be interpreted as the result of throw transfer processes (and associated throw gradients) in an area affected by a relay zone internally characterised by a zone of antithetic faulting, as well as by a pair of fault segments both associated with a downward, rather rapid decrease in throw.

It is well known that displacement gradients can be accommodated in several ways, depending on whether normal faults are isolated or in pairs, and on whether they are analysed in map or cross-section views (Walsh and Watterson, 1989; Walsh et al., 1999; Camanni et al., 2019; Nicol et al., 2020). In cross-section, displacement gradients are commonly accommodated by volumetric changes of the layers of the faulted sequence (Walsh et al., 1999; Rykkelid and Fossen, 2002; Camanni et al., 2019), and can be associated with areas of antithetic faulting (Mandl, 1987; Ferril and Morris, 2008; Childs et al., 2009; Ferrill et al., 2011; Zaky, 2017; Nixon et al., 2018; Nabavi et al., 2020). We interpret the significant thickness of the zone of fracturing in the hanging wall of fault zone-bounding fault segment Flt1 and in the central part of fault zone-bounding fault segment Flt5 to be the result of these strain localisation processes.

Finally, the above-described areas of increased fracture density considerable as fault-related are very localised and likely developed in response to local strains that are not necessarily reflecting the overall strain field that led to the development of the fault zone. For example, at branch points between fault segments with opposed dips, we expect

fractures to develop in a radial way. Similarly, fractures due to shearing between antithetic faults are not expected to have necessarily all the same orientation. This could justify the dispersion of the poles of the fractures within the study area (Fig. 5 inset) and their departure from parallelism with the N–S faults to which they relate.

6. Implications and conclusions

How the density of fault-related fractures may relate to the full range of structural complexities that fault zones can display at their interior is relatively poorly explored in the literature. This poor exploration could be due to, (i) the fact that circumstances in which fault zones can be observed in detail and in their full width for a significant portion of their strike or dip extents are relatively rare, and/or (ii) the fact that as displacement is progressively accumulated, fault displacement may localise on a single slip surface and the initial structural complexities of the fault zone can be obliterated and/or bypassed (e.g., Walsh et al., 2001; Childs et al., 2009; Delogkos et al., 2017b).

The high-resolution data analysed in this article allowed us to study in detail an incipient fault zone that still preserves a significant degree of structural complexities, and to relate these complexities to the density of fault-related fractures. Areas of denser fracturing are very localised and coincide with: (1) rock volumes bounded by antithetic faults developed within fault zones (Fig. 7A); (2) branch points between antithetic faults within the interior of fault zones and fault zone-bounding fault segments (Fig. 7B); (3) fault zone-bounding fault segments associated with significant displacement gradients (Fig. 7C); (4) relay zones between subordinate synthetic faults (Fig. 7D).

These results may aid prediction of the location of areas of fracturing within seismically mapped fault zones similar in structure to the one studied in this article. Fracturing associated with faulting is often below the resolution of the seismic reflection data and therefore cannot be readily detected and estimated using this technique. Accurately predicting fracture densities may be of pivotal importance for industrial applications that deal with sub-surface data, since regions of fracturing in fault zones are often demonstrated to be rock volumes of enhanced permeability (e.g., Caine et al., 1996; Evans et al., 1997; Agosta, 2008; Faulkner et al., 2010; Bense et al., 2013; Gillespie et al., 2020; Scibek, 2020; Michie et al., 2021; Boersma et al., 2021; Smeraglia et al., 2021). Therefore, being able to predict their location can have very significant implications for better understanding and even predicting fluid flow within faulted reservoirs for a wide range of practical applications, from CO_2 and energy (H_2) storage, to geothermal and hydrocarbon exploration and production, to mining and civil engineering.

Author statement

Giovanni Camanni: Conceptualization; Data curation; Formal analysis; Investigation; Visualization; Supervision; Methodology; Roles/Writing - original draft.

Francesco Vinci: Software; Data curation; Formal analysis; Investigation; Methodology; Visualization; Writing - review & editing.

Stefano Tavani: Software; Investigation; Methodology; Visualization; Writing - review & editing.

Valeria Ferrandino: Formal analysis; Investigation; Visualization

Stefano Mazzoli: Funding acquisition; Project administration; Writing - review & editing.

Amerigo Corradetti: Software; Investigation; Methodology; Writing - review & editing.

Mariano Parente: Funding acquisition; Project administration; Writing - review & editing.

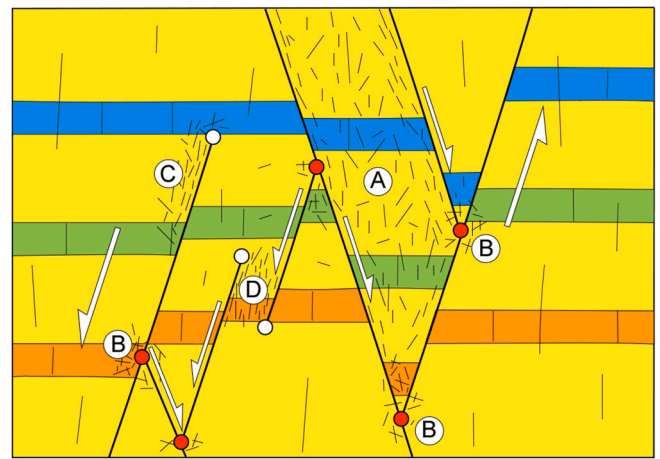Alessandro Iannace: Funding acquisition; Project administration; Writing - review & editing.

Fig. 7. Schematic 2D sketch showing the spatial distribution of the areas of denser fracturing within an incipient, complex fault zone similar to that of this study. White dots show fault tip points, whereas red dots are branch points between opposed-dipping faults. Note how areas of denser fracturing are rather localised and coincide with (i) rock volumes bounded by antithetic faults developed within the fault zone (e.g., A), (ii) branch points between these antithetic faults and fault zone-bounding fault segments (e.g., B, note that for illustrating purposes also other branch points between opposed-dipping faults at the interior of the fault zone are here interpreted as loci of dense fracturing), (iii) fault zone-bounding fault segments associated with significant displacement gradients (e.g., C), and (iv) relay zones between subordinate synthetic faults (e.g., D). (For interpretation of the references to colour in this figure legend, the reader is referred to the Web version of this article.)

Declaration of competing interest

The authors declare that they have no known competing financial interests or personal relationships that could have appeared to influence the work reported in this paper.

Appendix A. Supplementary data

Supplementary data to this article can be found online at https://doi.org/10.1016/j.jsg.2021.104432.

References

Aarland, R.K., Skjerven, J., 1998. Fault and fracture characteristics of a major fault zone in the northern North Sea: analysis of 3D seismic and oriented cores in the Brage Field (Block 31/4). Geological Society, London, Special Publications 127, 209–229.

Agosta, F., 2008. Fluid flow properties of basin-bounding normal faults in platform carbonates. Fucino Basin, central Italy. Geological Society, London, Special Publications 299, 277–291.

Bense, V.F., Gleeson, T., Loveless, S.E., Bour, O., Scibek, J., 2013. Fault zone hydrogeology. Earth Sci. Rev. 127, 171–192.

Boersma, Q.D., Bruna, P.O., de Hoop, S., Vinci, F., Tehrani, A.M., Bertotti, G., 2021. The impact of natural fractures on heat extraction from tight Triassic sandstones in the West Netherlands Basin: a case study combining well, seismic and numerical data. Neth. J. Geosci. 100.

Caiazzo, C., Cinque, A., Merola, D., 2000. Relative chronology and kinematics of the NW and NE trending faults of the Sorrento peninsula (southern apennines). Mem. Soc. Geol. It. 55, 165–174.

Caine, J.S., Evans, J.P., Forster, C.B., 1996. Fault zone architecture and permeability structure. Geology 24, 1025–1028.

Camanni, G., Roche, V., Childs, C., Manzocchi, T., Walsh, J., Conneally, J., Saqab, M.M., Delogkos, E., 2019. The three-dimensional geometry of relay zones within segmented normal faults. J. Struct. Geol. 129, 103895.

Carannante, G., Ruberti, D., Sirna, M., 2000. Upper Cretaceous ramp limestones from the Sorrento Peninsula (southern Apennines, Italy): micro- and macrofossil associations and their significance in the depositional sequences. Sediment. Geol. 132, 89–123.

Cello, G., Mazzoli, S., 1999. Apennine tectonics in southern Italy: a review. J. Geodyn. 27, 191–211.

Childs, C., Watterson, J., Walsh, J.J., 1995. Fault overlap zones within developing normal fault systems. J. Geol. Soc. 152, 535–549.

Childs, C., Watterson, J., Walsh, J.J., 1996. A model for the structure and development of fault zones. J. Geol. Soc. London 153, 337–340.

Childs, C., Manzocchi, T., Walsh, J.J., Bonson, C.G., Nicol, A., Schöpfer, M.P.J., 2009. A geometric model of fault zone and fault rock thickness variations. J. Struct. Geol. 31, 117–127.

Corradetti, A., Tavani, S., Parente, M., Iannace, A., Vinci, F., Pirmez, C., Torrieri, S., Giorgioni, M., Pignalosa, A., Mazzoli, S., 2018. Distribution and arrest of vertical through-going joints in a seismic-scale carbonate platform exposure (Sorrento peninsula, Italy): insights from integrating field survey and digital outcrop model. J. Struct. Geol. 108, 121–136. https://doi.org/10.1016/j.jsg.2017.09.009.

Crider, J.G., Pollard, D.D., 1998. Fault linkage: three-dimensional mechanical interaction between echelon normal faults. J. Geophys. Res.: Solid Earth 103, 24373–24391.

D'Argenio, B., Pescatore, T., Scandone, P., 1975. Structural pattern of the campania-lucania apennines, in structural model of Italy. Quad. Ric. Sci. 90, 313–327.

De Castro, P., 1962. Il Giura-Lias dei Monti Lattari e dei rilievi ad ovest della Valle dell'Irno e della Piana di Montoro. Bollettino della Soc. dei Nat. Napoli 71, 3–34.

Delogkos, E., Childs, C., Manzocchi, T., Walsh, J.J., Pavlides, S., 2017a. The role of bed-parallel slip in the development of complex normal fault zones. J. Struct. Geol. https://doi.org/10.1016/j.jsg.2017.02.014.

Delogkos, E., Manzocchi, T., Childs, C., Sachanidis, C., Barbas, T., Schöpfer, M.P., Chatzipetros, A., Pavlides, S., Walsh, J.J., 2017b. Throw partitioning across normal fault zones in the Ptolemais Basin, Greece. In: Childs, C., Holdsworth, R.E., Jackson, C.A.-L., Manzocchi, T., Walsh, J.J., Yielding, G. (Eds.), The Geometry and Growth of Normal Faults, vol. 439. Geological Society of London, Special Publication.

Delogkos, E., Childs, C., Manzocchi, T., Walsh, J.J., 2018. The nature and origin of bed-parallel slip in Kardia mine, Ptolemais Basin, Greece. J. Struct. Geol. 113, 115–133.

Delogkos, E., Manzocchi, T., Childs, C., Camanni, G., Roche, V., 2020. The 3D structure of a normal fault from multiple outcrop observations. J. Struct. Geol. 136.

Demurtas, M., Fondriest, M., Balsamo, F., Clemenzi, L., Storti, F., Bistacchi, A., Di Toro, G., 2016. Structure of a normal seismogenic Fault zone in carbonates: the vado di Corno fault, campo imperatore, central apennines (Italy). J. Struct. Geol. 90, 185–206.

Dershowitz, W.S., Herda, H.H., 1992. Interpretation of fracture spacing and intensity. In: The 33th US Symposium on Rock Mechanics (USRMS). American Rock Mechanics Association.

Evans, J.P., Forster, C.B., Goddard, J.V., 1997. Permeability of fault-related rocks, and implications for hydraulic structure of fault zones. J. Struct. Geol. 19 (11), 1393–1404.

Faulkner, D.R., Lewis, A.C., Rutter, E.H., 2003. On the internal structure and mechanics of large strike-slip fault zones: field observations of the Carboneras fault in southeastem Spain. Tectonophysics 367 (3e4), 235e251.

Faulkner, D.R., Jackson, C.A.L., Lunn, R.J., Schlische, R.W., Shipton, Z.K., Wibberley, C.A.J., Withjack, M.O., 2010. A review of recent developments concerning the structure, mechanics and fluid flow properties of fault zones. J. Struct. Geol. 32, 1557–1575.

Ferrill, D.A., Morris, A.P., 2008. Fault zone deformation controlled by carbonate mechanical stratigraphy, Balcones fault system, Texas. AAPG (Am. Assoc. Pet. Geol.) Bull. 92 (3).

Ferrill, D.A., Morris, A.P., McGinnis, R.N., Smart, K.J., Ward, W.C., 2011. Fault zone deformation and displacement partitioning in mechanically layered carbonates: the Hidden Valley fault, central Texas. AAPG (Am. Assoc. Pet. Geol.) Bull. 95, 1383–1397.

Fossen, H., Johansen, T.E.S., Hesthammer, J., Rotevatn, A., 2005. Fault interaction in porous sandstone and implications for reservoir management; examples from southern Utah. AAPG (Am. Assoc. Pet. Geol.) Bull. 89 (12), 1593–1606.

Gillespie, P.A., Holdsworth, R.E., Long, D., Williams, A., Gutmanis, J.C., 2020. Introduction: geology of fractured reservoirs. J. Geol. Soc. 178.

Guerriero, V., Iannace, A., Mazzoli, S., Parente, M., Vitale, S., Giorgioni, M., 2010. Quantifying uncertainties in multi-scale studies of fractured reservoir analogues : implemented statistical analysis of scan line data from carbonate rocks. J. Struct. Geol. 32, 1271–1278.

Guerriero, V., Vitale, S., Ciarcia, S., Mazzoli, S., 2011. Improved statistical multi-scale analysis of fractured reservoir analogues. Tectonophysics 504, 14–24.

Healy, D., Rizzo, R.E., Cornwell, D.G., Farrell, N.J.C., Watkins, H., Timms, N.E., Gomez-Rivas, E., Smith, M., 2017. FracPaQ: a MATLABTM toolbox for the quantification of fracture patterns. J. Struct. Geol. 95, 1–16.

Huggins, P., Watterson, J., Walsh, J.J., Childs, C., 1995. Relay zone geometry and displacement transfer between normal faults recorded in coal-mine plans. J. Struct. Geol. 17, 1741–1755.

Iannace, A., 1993. Caratteri diagenetici dei carbonati di Piattaforma dell'Appennino Meridionale e loro implicazioni paleogeografiche. Riv. Ital. Paleontol. Stratigr. 99, 57–80.

Iannace, A., Capuano, M., Galluccio, L., 2011. "Dolomites and dolomites" in Mesozoic platform carbonates of the Southern Apennines: geometric distribution, petrography and geochemistry. Palaeogeogr. Palaeoclimatol. Palaeoecol. 310, 324–339.

Iannace, A., Frijia, G., Galluccio, L., Parente, M., 2014. Facies and early dolomitization in Upper Albian shallow-water carbonates of the southern Apennines (Italy): paleotectonic and paleoclimatic implications. Facies 60, 169–194.

Ispra, 2016. Carta Geologica d'Italia Alla Scala 1:50.000, Foglio 466 "Sorrento".

Kristensen, M.B., Childs, C.J., Korstgård, J.A., 2008. The 3D geometry of small-scale relay zones between normal faults in soft sediments. J. Struct. Geol. 30, 257–272.

Mandl, G., 1987. Tectonic deformation by rotating parallel faults: the "bookshelf" mechanism. Tectonophysics 141 (4).

Marchal, D., Guiraud, M., Rives, T., 2003. Geometric and morphologic evolution of normal fault planes and traces from 2D to 4D data. J. Struct. Geol. 25, 135–158.

Mauldon, M., Dunne, W.M., Rohrbaugh, M.B.J., 2001. Circular scanlines and circular windows: new tools for characterizing the geometry of fracture traces. J. Struct. Geol. 23, 247–258.

Menardi Noguera, A., Rea, G., 2000. Deep structure of the campanian-lucanian arc (southern apennine, Italy). Tectonophysics 324 (4), 239–265.

Mercuri, M., Carminati, E., Tartarello, M.C., Brandano, M., Mazzanti, P., Brunetti, A., McCaffrey, K.J.W., Collettini, C., 2020. Lithological and structural control on fracture frequency distribution within a carbonate-hosted relay ramp. J. Struct. Geol. 137.

Michie, E.A.H., 2015. Influence of host lithofacies on fault rock variation in carbonate fault zones: a case study from the Island of Malta. J. Struct. Geol. 76, 61–79.

Michie, E.A.H., Haines, T.J., 2016. Variability and heterogeneity of the petrophysical properties of extensional carbonate fault rocks, Malta. Petrol. Geosci. 22 (2), 136–152.

Michie, E.A.H., Kaminskaite, I., Cooke, A.P., Fisher, Q.J., Yielding, G., Tobiss, S.D., 2021. Along-strike permeability variation in carbonate-hosted fault zones. J. Struct. Geol. 142.

Milia, A., Torrente, M., 1997. Evoluzione tettonica della Penisola sorrentina. Boll. Soc. Geol. It 116, 487–502.

Nabavi, S.T., Alavi, S.A., Wibberley, C.A.J., Jahangiri, M., 2020. Normal fault networks and their spatial relationships in Plio-Quaternary sedimentary series: a case study in the Zanjan Depression, NW Iran. J. Struct. Geol. 136.

Nicol, A., Childs, C., Walsh, J.J., Manzocchi, T., Schöpfer, M.P.J., 2016. Interactions and growth of faults in an outcrop-scale system. In: Childs, C., Holdsworth, R.E., Jackson, C.A.-L., Manzocchi, T., Walsh, J.J., Yielding, G. (Eds.), The Geometry and Growth of Normal Faults, vol. 439. Geological Society of London, Special Publication. https://doi.org/10.1144/SP439.9.

Nicol, A., Walsh, J.J., Childs, C., Manzocchi, T., 2020. The growth of faults. In: Tanner, D., Brandes, C. (Eds.), Understanding Faults: Detecting, Dating, and Modeling. Elsevier.

Nixon, W.C., Vaagan, S., Sanderson J., D., Gawthorpe L., R., 2018. Spatial distribution of damage and strain within a normal fault relay at Kilve, U.K. J. Struct. Geol. 118, 194–209.

Nixon, C.W., Nærland, K., Rotevatn, A., Dimmen, V., Sanderson, D.J., Kristensen, T.B., 2020. Connectivity and network development of carbonate-hosted fault damage zones from western Malta. J. Struct. Geol. 141.

Peacock, D.C.P., Sanderson, D.J., 1991. Displacements, segment linkage and relay ramps in normal fault zones. J. Struct. Geol. 13 (6), 721–733.

Peacock, D.C.P., Sanderson, D.J., 1994. Geometry and development of relay ramps in normal fault systems. AAPG (Am. Assoc. Pet. Geol.) Bull. 78, 147–165.

Peacock, D.C.P., Knipe, R.J., Sanderson, D.J., 2000. Glossary of normal faults. J. Struct. Geol. 22, 291–305.

Peacock, D.C.P., 2002. Propagation, interaction and linkage in normal fault systems. Earth Sci. Rev. 58, 121–142.

Perriello Zampelli, S., De Vita, P., Imbriaco, D., Calcaterra, D., 2015. Engineering geology for society and territory – volume 2: landslide processes. In: Lollino, G., Giordan, D., Crosta, G.B., Corominas, J., Azzam, R., Wasowski, J., Sciarra, N. (Eds.), Engineering Geology for Society and Territory - Volume 2. Landslide Processes, pp. 813–816.

Remondino, F., El-Hakim, S., 2006. Image-based 3D modelling: a review. Photogramm. Rec. 21, 269–291.

Robson, D., 1987. Depositional models for some cretaceous carbonates from the Sorrento peninsula, Italy. Memor. Soc. Geol. Ital. 40, 251–257.

Roche, V., Childs, C., Madritsch, H., Camanni, G., 2020. Layering and structural inheritance controls on fault zone structure in three dimensions: a case study from the northern Molasse Basin, Switzerland. J. Geol. Soc. 177, 493–508.

Roche, V., Camanni, G., Delogkos, E., Childs, C., Manzocchi, T., Walsh, J., Conneally, J., Saqab, M., Delogkos, E., 2021. Variability in the three-dimensional geometry of segmented normal fault surfaces. Earth Sci. Rev. 216.

Rohrbaugh Jr., M.B., Dunne, W.M., Mauldon, M., 2002. Estimating fracture trace intensity, density, and mean length using circular scan lines and windows. AAPG Bull. 86 (12), 2089–2104.

Roure, F., Casero, P., Vially, R., 1991. Growth processes and melange formation in the southern Apennines accretionary wedge. Earth Planet Sci. Lett. 102, 395–412.

Rotevatn, A., Fossen, H., Hesthammer, J., Aas, T.E., Howell, J.A., 2007. Are relay ramps conduits for fluid flow? Structural analysis of a relay ramp in Arches National Park, Utah. Geological Society, London, Special Publications 270, 55–71.

Rykkelid, E., Fossen, H., 2002. Layer rotation around vertical fault overlap zones: observations from seismic data, field examples, and physical experiments. Mar. Petrol. Geol. 19, 181–192.

8

Scibek, J., 2020. Multidisciplinary database of permeability of fault zones and surrounding protolith rocks at world-wide sites. Sci Data 7, 95.

Smeraglia, L., Giuffrida, A., Grimaldi, S., Pullen, A., La Bruna, V., Billi, A., Agosta, F., 2021. Fault-controlled upwelling of low-T hydrothermal fluids tracked by travertines in a fold-and-thrust belt, Monte Alpi, southern apennines, Italy. J. Struct. Geol. 144, 104276.

Soliva, R., Benedicto, A., 2004. A linkage criterion for segmented normal faults. J. Struct. Geol. 26 (12), 2251–2267.

Tavani, S., Arbues, P., Snidero, M., Carrera, N., Muñoz, J.A., 2011. Open Plot Project: an open-source toolkit for 3-D structural data analysis. Solid Earth 2, 53–63.

Van der Zee, W., Wibberley, C.A.J., Urai, L.J., 2008. The influence of layering and pre-existing joints on the development of internal structure in normal fault zones: the Lodeve basin, France. Geological Society, London, Special Publications 299, 57–74.

Vinci, F., Iannace, A., Parente, M., Pirmez, C., Torrieri, S., Giorgioni, M., 2017. Early dolomitization in the lower cretaceous shallow-water carbonates of southern apennines (Italy): clues about palaeoclimatic fluctuations in western tethys. Sediment. Geol. 362, 17–36.

Walsh, J.J., Watterson, J., 1989. Displacement gradients on fault surfaces. J. Struct. Geol. 11, 307–316.

Walsh, J.J., Watterson, J., 1991. Geometric and kinematic coherence and scale effects in normal fault systems. In: Roberts, A.M., Yielding, G., Freeman, B. (Eds.), The Geometry of Normal Faults, vol. 56. Geological Society of London, Special Publication, pp. 193–203.

Walsh, J.J., Watterson, J., Bailey, W.R., Childs, C., 1999. Fault relays, bends and branch-lines. J. Struct. Geol. 21 (8–9), 1019–1026.

Walsh, J.J., Childs, C., Meyer, V., Manzocchi, T., Imber, J., Nicol, A., Tuckwell, G., Bailey, W.R., Bonson, C.G., Watterson, J., Nell, P.A.R., Strand, J.A., 2001. Geometrical controls on the evolution of normal fault systems. In: Holdsworth, R.E., Strachan, R.A., Magloughlin, J.F., Knipe, R.J. (Eds.), The Nature of the Tectonic Significance of Fault Zone.

Walsh, J.J., Bailey, W.R., Childs, C., Nicol, A., Bonson, C.G., 2003. Formation of segmented normal faults: a 3-D perspective. J. Struct. Geol. 25, 1251–1262.

Westoby, M.J., Brasington, J., Glasser, N.F., Hambrey, M.J., Reynolds, J.M., 2012. "Structure-from-Motion" photogrammetry: a low-cost, effective tool for geoscience applications. Geomorphology 179, 300–314.

Zaky, K.S., 2017. fault zone architecture within miocene–pliocene syn-rift sediments, northwestern red sea, Egypt. J. Earth Syst Sci. 126.

Zeeb, C., Gomez-Rivas, E., Bons, P.D., Blum, P., 2013. Evaluation of sampling methods for fracture network characterization using outcrops. AAPG Bull. 97 (9), 1545–1566.